A simple relationship between volcanic sulfate aerosol optical depth and surface temperature change simulated in an atmosphere-ocean general circulation model.

A simple relationship between volcanic sulfate aerosol optical depth and surface temperature change simulated in an atmosphere-ocean general circulation model

B. M. Harris[1] and E. J. Highwood[1]

Received 4 June 2010; revised 31 October 2010; accepted 4 November 2010; published 8 March 2011.

[1] In this study we quantify the relationship between the aerosol optical depth increase from a volcanic eruption and the severity of the subsequent surface temperature decrease. This investigation is made by simulating 10 different sizes of eruption in a global circulation model (GCM) by changing stratospheric sulfate aerosol optical depth at each time step. The sizes of the simulated eruptions range from Pinatubo-sized up to the magnitude of supervolcanic eruptions around 100 times the size of Pinatubo. From these simulations we find that there is a smooth monotonic relationship between the global mean maximum aerosol optical depth anomaly and the global mean temperature anomaly and we derive a simple mathematical expression which fits this relationship well. We also construct similar relationships between global mean aerosol optical depth and the temperature anomaly at every individual model grid box to produce global maps of best-fit coefficients and fit residuals. These maps are used with caution to find the eruption size at which a local temperature anomaly is clearly distinct from the local natural variability and to approximate the temperature anomalies which the model may simulate following a Tambora-sized eruption. To our knowledge, this is the first study which quantifies the relationship between aerosol optical depth and resulting temperature anomalies in a simple way, using the wealth of data that is available from GCM simulations.

Citation: Harris, B. M., and E. J. Highwood (2011), A simple relationship between volcanic sulfate aerosol optical depth and surface temperature change simulated in an atmosphere-ocean general circulation model, *J. Geophys. Res.*, *116*, D05109, doi:10.1029/2010JD014581.

1. Introduction

[2] Large volcanic eruptions can eject sulfur dioxide into the stratosphere where it reacts with water vapor to produce highly scattering sulfate aerosol droplets, raising planetary albedo and leading to a radiative cooling of the Earth's surface [*Robock*, 2000]. The local and regional cooling following large volcanic eruptions has historically been documented by interested observers in various places across the globe [*Oppenheimer*, 2003; *Thordarson and Self*, 2003] and, in recent years, the global pattern of cooling has been recorded by satellite instruments [*Bluth et al.*, 1992; *Minnis et al.*, 1993]. These historic and satellite-based observations have been combined by a few authors [*Pollack et al.*, 1976; *Sigurdsson*, 1990; *Rampino and Self*, 1993] to quantify the relationship between volcanic emissions and atmospheric cooling. It is these relationships, based on extrapolating the trend from small emission masses which were, until recently, used to estimate the cooling which may occur following the largest "supervolcanic" eruptions [see, e.g., *Zielinski et al.*, 1996; *Ambrose*, 1998; *Oppenheimer*, 2002].

[3] Another source of information on postvolcanic cooling, as well as a myriad of other processes, comes from global circulation models (GCM), which have been used to conduct simulations of specific historic eruptions, such as the eruption of Mt Pinatubo in June 1991 [*Kirchner et al.*, 1999; *Ramachandran et al.*, 2000; *Stenchikov et al.*, 2002]. These model simulations have been used to estimate the mitigating effect of volcanic eruptions on global warming [*Rind et al.*, 1992; *Hansen et al.*, 1992; *Tett et al.*, 2002; *Gleckler et al.*, 2006; *Schneider et al.*, 2009] as well as used to analyze and improve model representations of particular processes such as the dynamical Eurasian winter warming [*Labitzke and van Loon*, 1989; *Robock and Mao*, 1992; *Graf et al.*, 1993; *Kodera*, 1994; *Shindell et al.*, 2004; *Fischer et al.*, 2007; *Stenchikov et al.*, 2006; *Christiansen*, 2007] or the chemical evolution of the volcanic emissions [*Stenchikov et al.*, 1998; *Timmreck et al.*, 1999, 2009; *Timmreck and Graf*, 2000; *Niemeier et al.*, 2009]. More recently GCMs have also simulated supervolcanic eruptions [*Jones et al.*, 2005; *Robock et al.*, 2009] and the surface temperature anomalies produced by these supervolcanic simulations were generally much larger than the anomalies calculated using the relationships derived from historical eruptions. To date, however, this wealth of simulations has not been used to

[1]Department of Meteorology, University of Reading, Reading, UK.

0148-0227/11/2010JD014581

frame a relationship between volcanic emission size and surface temperature anomalies.

[4] GCM simulations are an excellent tool for creating such a relationship. First, it is possible to simulate very high emissions in GCMs thereby removing the need to extrapolate the relationship, which otherwise intrinsically assumes that the response follows the same trend for smaller eruptions as it does for the largest. Second, is it possible to extract not only the global mean postvolcanic temperature anomalies from climatic noise with a good degree of reliability, but it is also possible to extract regional temperature anomalies at the grid box scale, information which is not easy to extract from observations of historic eruptions. This second point is important because observations of historic eruptions and paleoclimatic reconstructions from proxy data are primarily drawn from single point locations. The ability to analyze the temperature changes which are consistent across regions of a few model grid boxes holds great potential for facilitating a user-friendly comparison between modeling and observation data.

[5] This paper details the method and uses of producing user-friendly GCM-based relationships between surface temperature anomalies and volcanic emissions on both global mean and grid box scales. Section 2 outlines our method of simulating volcanic eruptions in HadCM3, a fully coupled atmosphere-ocean GCM, by changing the sulfate aerosol optical depth of the model. Section 3.1 describes the derivation of the global-mean relationship using a range of different aerosol optical depth anomalies. Section 3.2 describes the formation of regional relationships between temperature anomaly and eruption size and discusses their potential applications. Section 4 includes a discussion of the limitations of the data presented here.

2. GCM Simulations of Large Volcanic Eruptions

[6] We have used the UK Met Office Atmosphere-Ocean General Circulation Model, HadCM3 to simulate generic volcanic eruptions. The atmosphere component of the model has a horizontal grid resolution of 2.5° × 3.75° latitude × longitude and 19 levels in the vertical up to a model top of 10 hPa [*Pope et al.*, 2000] The ocean component has a horizontal grid resolution of 1.25° × 1.25° latitude × longitude and 20 levels in the vertical, with the highest resolution concentrated in the upper layers [*Gordon et al.*, 2000]. This model has a climate sensitivity of 3–3.3 K in response to a doubling of CO_2 [*Gregory et al.*, 2004; *Randall et al.*, 2007] which straddles the mean value of 3.2 K found in the IPCC AR4 for 23 GCMs and is well within the range of observationally derived values of 2.0–4.5 K as found, again, in the IPCC AR4 [*Randall et al.*, 2007; *Hegerl et al.*, 2007]. HadCM3 has been used extensively in the third and fourth IPCC Assessment Reports [*Houghton et al.*, 2001; *Solomon et al.*, 2008] as well as numerous other studies of the current, past, and future climate of the Earth [*Stott et al.*, 2000; *Hewitt et al.*, 2001; *Tett et al.*, 2002; *Johns et al.*, 2003; *Stainforth et al.*, 2005]. It was used by *Jones et al.* [2005] to perform the first fully coupled GCM simulation of a supervolcanic eruption. In addition to global mean changes, HadCM3 has been shown to simulate regional climate variations such as sea ice distribution, ENSO and the Asian Summer Monsoon with a fair degree of accuracy [*Gordon et al.*, 2000; *Collins et al.*, 2001; *Turner et al.*, 2005]. There are, however, a couple of limitations to the model which will impact the postvolcanic temperature response. First, the model top is low at 10 hPa and, second, there is no interactive evolution of atmospheric chemistry, including ozone. The potential impacts of these limitations on the values to be presented here are returned to in section 4.

[7] The HadCM3 model is used to conduct 15 simulations of different sized eruptions using the same technique as [*Jones et al.*, 2005]. These simulations are driven by increasing sulfate aerosol loading in the stratosphere at each time step to represent simplistically the processes of aerosol formation and sedimentation, which are not handled automatically by the model. The sulfate aerosol used is one of five "climatological" aerosols used by HadCM3 [*Cusack et al.*, 1998] and as such it has a fixed unimodal log normal size distribution with a geometric radius of $r_g = 0.07$ μm and a standard deviation of $\sigma = 1.86$ as well as fixed optical properties, a single scattering albedo of $\omega = 0.9999$ and an asymmetry factor of $g = 0.7$ at a wavelength of $\lambda = 0.55$ μm [*World Meteorological Organization*, 1983]. These sizes and optical properties of the sulfate aerosol do not change throughout the simulation, which leads to inaccuracies in the behavior of the volcanic sulfate aerosol in the model, particularly for large eruption sizes. For example, aerosol sizes were observed to increase following the Pinatubo eruption [*Sato et al.*, 1993; *Stenchikov et al.*, 1998; *Niemeier et al.*, 2009] and this in turn would tend to reduce scattering in the shortwave and increase longwave absorption, resulting in lower temperature anomalies [*Timmreck et al.*, 2009]. Furthermore, there is no representation of the chemical or microphysical interactions of the sulfate aerosol [*Pinto et al.*, 1989; *Bekki*, 1995; *Timmreck and Graf*, 2000] and so the lifetime of the aerosol is the same in all simulations. The impacts of these important limitations are somewhat reduced here as we drive and analyze our simulations with respect to the aerosol optical depth anomaly at 0.55 μm produced by the sulfate aerosol rather than by what type and how much of the aerosol is created. In doing so, we are simulating a simple and generic "Pinatubo-like" eruption, rather than attempting to simulate any specific historic eruptions.

[8] The optical depth anomalies used to drive the simulations of eruptions are designed to be a similar size and distribution to the post-Pinatubo optical depth anomalies at 0.55 μm in the Sato Index [*Sato et al.*, 1993; *Robock*, 2000], as shown in Figure 1. The Sato Index was also used in four broad latitudinal bands used by *Jones et al.* [2005], though here we used a higher latitudinal resolution. The mass of sulfate aerosol required in each vertical column of the model to create this required optical depth is calculated using the extinction coefficient of the sulfate aerosol at 0.55 μm and a conversion from *Slingo* [1989] to account for the broad spectral bands of the model's radiation code. Once calculated, this mass of aerosol is then distributed throughout the model stratosphere with a uniform mass mixing ratio.

[9] The 15 simulations consist of a sulfate-aerosol free control run, a five-member ensemble simulation of a Pinatubo-sized eruption, and a further nine simulations of larger eruptions. The 50-year control run is started under fully equilibrated initial conditions representative of January 2000, following which the climatic conditions of the simulations are not forced to follow any observational or his-

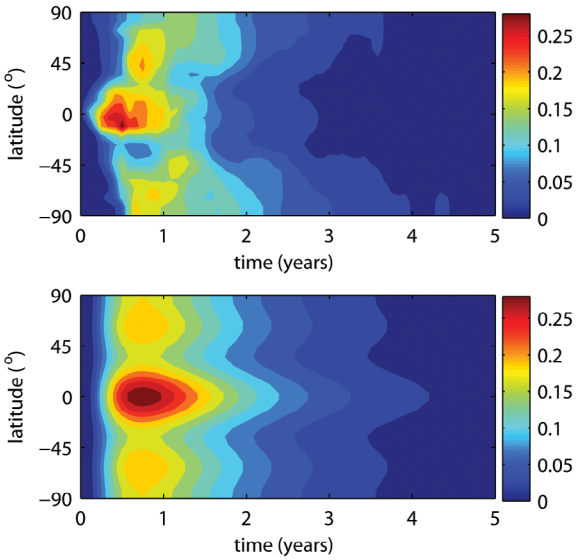

Figure 1. Total column sulfate aerosol optical depth increases at 0.55 μm following the Pinatubo eruptions from (top) the Sato Index [*Sato et al.*, 1993] and (bottom) the similar distribution implemented in the HadCM3 model by changing stratospheric climatological sulfate aerosol concentrations.

torical records, but allowed to evolve freely in response to the model's own internal variability. A base Pinatubo-sized ensemble member is constructed from the control run by initiating the start of the eruption five years after the beginning of the simulation and allowing the model to respond freely to this sulfate-aerosol forcing for 30 more years. The remaining four ensemble members are created by initiating the start of the eruption in successive years. For the larger eruptions, the relative latitudinal and temporal distribution of aerosol optical depth anomalies at 0.55 μm remains identical to the base ensemble member while the total amount of the sulfate aerosol in the model is increased in each simulation by multiplying the aerosol optical depth in each grid box by a scaling factor (3, 5, 10, 15, 20, 40, 60, 80 and 100). Each simulation of these larger eruptions is a single run. It is possible, in light of the work by *Niemeier et al.* [2009], that the optical depth anomalies which we are simulating in the largest eruptions are unobtainable large but it is beyond the scope of this study to ascertain an upper limit to the possible sulfate aerosol optical depth anomalies which can be produced volcanic eruptions. As the eruption sizes are changed by changing the optical depth anomalies then hereafter the term "eruption size" strictly describes the size of the optical depth perturbation.

[10] Figure 2 shows the results from the five-member ensemble of HadCM3 simulations of the Pinatubo-sized

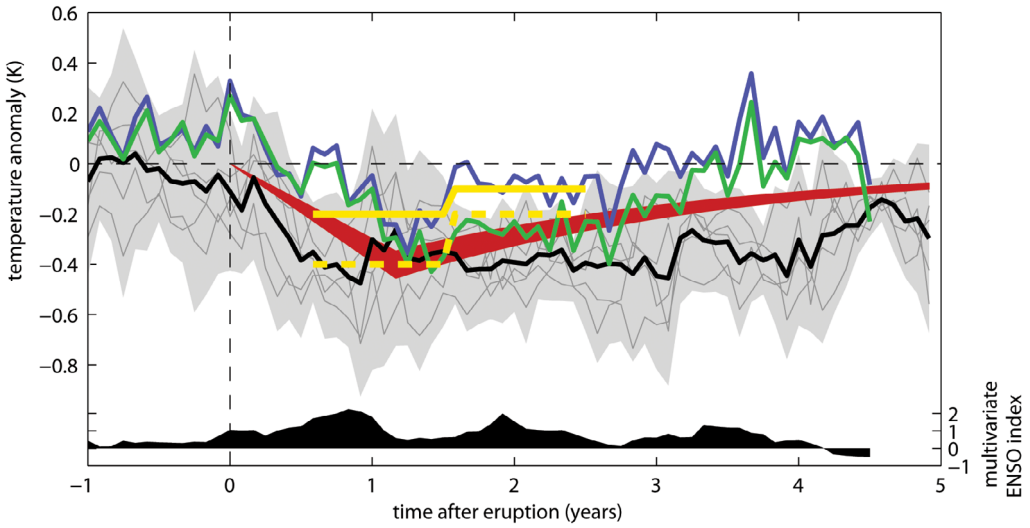

Figure 2. Changes to global mean surface temperatures following the Pinatubo eruption as simulated in the HadCM3 Pinatubo ensemble (gray lines denote individual run values, the black line shows the ensemble mean, and gray shading shows two standard deviations of the individual ensemble runs with respect to the ensemble mean); as documented in the ERA-40 reanalysis (blue); as documented in the NCEP/NCAR reanalysis (dark green); as observed by *McCormick et al.* [1995] with and without the effects of El Nino (dashed and solid yellow lines, respectively); and the range of post-Pinatubo surface temperature anomalies from nine different scenarios calculated by *Santer et al.* [2001] by using an iterative procedure to remove the temperature effects of ENSO from three different ENSO indices (SOI, NINO 3, NINO 3.4) and given three different pre-eruption averaging ranges for each index (red). The black filled shading using the right-hand axis shows the corresponding Multivariate ENSO Index *Wolter and Timlin* [1998; K. Wolter and M. Timlin, Monitoring ENSO in COADS with a seasonally adjusted principal component index, paper presented at the 17th Climate Diagnostics Workshop, Okla. Clim. Surv., Norman, Okla., 1993] which indicates the strength of El Nino (positive)/La Nina (negative) events.

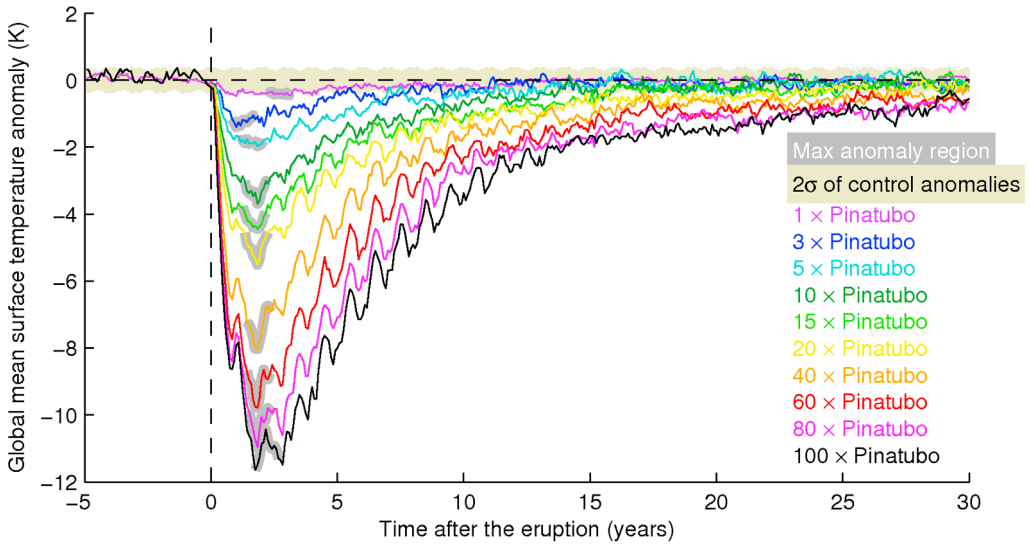

Figure 3. Time series of global mean surface temperature anomalies following volcanic eruptions with aerosol optical depth anomalies ranging in size from 1 to 100 × Pinatubo. The gray-yellow shading outlines two standard deviations of the interannual monthly surface temperature anomalies in the control run with respect to the climatology of that run. The gray shading over each eruption's time series highlights the continuous 12-month period where the highest global mean temperature anomalies are found.

eruptions as well as re-analysis data, observations published by *McCormick et al.* [1995] and ENSO-corrected observations by *Santer et al.* [2001]. The time series of the multivariate ENSO index is also shown. The most marked difference between the HadCM3 simulations and the observed temperature anomalies are that the model overestimates the timescale of cooling in comparison to the reanalysis products, taking approximately 10 years to return to equilibrium temperatures instead of 2. Aside from this, there is a good agreement in the magnitude of the post-volcanic temperature anomalies in the ensemble simulations and the reanalyses/observations when the effects of ENSO are taken into account. While HadCM3 is capable of simulating ENSO events, the climatic conditions of the model are not forced to represent those of the 1991 Pinatubo eruption and so the large El Nino which occurred around the time of Pinatubo (and the resulting increase in temperatures) is not present in the simulations. Both *McCormick et al.* [1995] and *Santer et al.* [2001] have calculated and removed the effect of ENSO from their observations of surface temperature anomalies and there is a good and clear agreement between these adjusted values and the model simulations. These results give us confidence that our model simulations of generic Pinatubo-sized eruptions are sufficient for constructing relationships between aerosol optical depth and surface temperature anomaly.

[11] Observational data is not available to check the sufficiency of the largest eruption simulations and so instead we draw comparison with the supervolcanic simulations of *Jones et al.* [2005] and *Robock et al.* [2009]. The temperature anomalies seen in the 100 × Pinatubo simulation are of a similar order of magnitude to those two studies. There is a very good agreement, to within a degree or so, between the simulations conducted here and the results of *Jones et al.* [2005], which is expected given the similarity of the experimental setup. To compare with *Robock et al.* [2009], we must first choose a metric by which to make that comparison, as their simulations are based on emissions of sulfur dioxide, rather than optical depth anomalies. We have chosen to compare eruptions which have similar incoming shortwave radiation anomalies (not shown for HadCM3) as this is a measure of changes in atmospheric transmission, though it is somewhat crude. Using this framework we find that the 2 Gt SO_2 and 6 Gt SO_2 simulations made by *Robock et al.* [2009] are comparable to the 60 × Pinatubo and 100 × Pinatubo experiments made here respectively. These two comparisons show that the simulations of *Robock et al.* [2009] are 3–4 K cooler than the simulations on HadCM3 and this temperature difference is around a degree larger in the comparison of the two bigger eruptions. This increase, although small, may be significant and is probably due to the extended lifetime of sulfate aerosol used by *Robock et al.* [2009], which will be discussed again in Section 4. We are confident that our simulations broadly agree with the two previous representations of a generic supervolcano and so we will use these values to form a simple relationship between aerosol optical depth and eruption size. We must stress, however, that these relationships are constructed strictly within the framework of Pinatubo-like eruptions on HadCM3 and may not be applicable to other model simulations or the real world.

3. Simplified Temperature Predictions

3.1. Global Mean

[12] Figure 3 shows the time series of global mean temperature anomalies following each of the volcanic eruptions simulated. It is clear that there is a monotonic relationship between eruption size and peak temperature anomaly, which is requisite for forming a simple relationship between volcanic aerosol optical depth and surface temperature anomaly. The maximum cooling following all eruptions

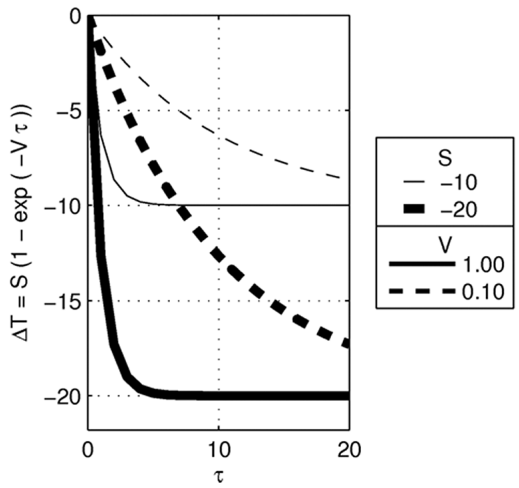

Figure 4. Schematic illustration of the effect of changing coefficients S and $\mathcal{V}$ in equation (1). $\mathcal{S}$ is the "saturation temperature anomaly" or the maximum value of ΔT which can be attained by an infinitely high value of τ. Changing $\mathcal{V}$ alters the rate at which the saturation temperature change is obtained with respect to increasing eruption size.

greater than Pinatubo-sized are distinct from interannual variability (as represented by two standard deviations of the global mean annual surface temperature anomalies in the control run) and the maximum temperature anomaly following the largest 100 × Pinatubo eruption is −11.5 K. Though there are changes in the timing of the peak cooling between eruption sizes, the timescales of temperature decrease and recovery are broadly similar for each of the eruptions. There are two clear differences in the temperature response to the larger and smaller aerosol optical depth anomalies. The first is the marked increase in interannual variability between around 3–12 years after the eruption. This increase is due to a combination of the slow summer melting of the boreal ice cap and the enhanced growth of the austral ice cap giving enhanced cooling toward the end of the year along with a large summer warming, winter cooling response from the boreal landmasses. This difference will not have an impact on a simple relationship if that relationship is built using annual or 12-month mean values. The second difference is the slower return of global mean surface temperatures to equilibrium following larger aerosol optical depth anomalies and it occurs because of extra cooling as the exaggerated growth of the ice sheets increases planetary albedo. We take this second difference into account later when choosing an appropriate way of averaging the time series anomalies.

[13] As the relationship between volcanic aerosol optical depth perturbation and temperature decrease is monotonic, we can construct a simple mathematical relation between the two. This relation is found by using the following nonlinear expression which includes the exponent of the global mean maximum optical depth anomaly:

$$\Delta T = \mathcal{S}[1 - \exp(-\tau\mathcal{V})] \quad (1)$$

ΔT is the global mean 12-month maximum postvolcanic surface temperature anomaly for an eruption with a global mean maximum optical depth of τ at 0.55 μm. Using this expression, $\mathcal{S}$ and $\mathcal{V}$ are found by an iterative Matlab code which calculates a nonlinear best fit using the Levenburg-Marquardt algorithm [*Seber and Wild*, 2003]. With values of $\mathcal{S}$ and $\mathcal{V}$ found in this way, the first four coefficients and residuals of the Taylor expansion of the subsequent relationship are almost identical to the coefficients and residuals of a third order polynomial fit to the model data, indicating that the goodness of this fit is almost identical to that which would be obtained by using a third-order polynomial. This form of expression has an advantage over a simple polynomial, however, in that its components provide us with information about the evolution of temperature anomalies with respect to global mean maximum volcanic aerosol optical depth changes. $\mathcal{S}$ is the "saturation temperature anomaly," a theoretical maximum global cooling for an infinite peak magnitude of aerosol optical depth anomalies. $\mathcal{V}$ defines the eruption size at which temperature anomalies approach the values of $\mathcal{S}$, as shown in Figure 4.

[14] To find values of $\mathcal{S}$ and $\mathcal{V}$, we have averaged ΔT over the 12-month peak temperature anomalies of each simulation before using the iterative fitting code. This period is highlighted for each eruption in Figure 3. By doing this we create a simple relationship which does not encompass temperature anomalies as they return to equilibrium. Such narrow focus is desirable as we have seen that the return to equilibrium temperatures is much longer in the model than observed for Pinatubo, and it is insensitive to the lag in the time of peak cooling following the largest aerosol optical depth anomalies. Furthermore, this relation captures the largest temperature anomalies which is arguably the diagnostic of greatest broad interest.

[15] Naturally, the temperature anomalies do not all fit the relationship derived by equation (1) perfectly and this is quantified by the value $2\sigma[res]$, or two standard deviations of the residuals between the global mean temperature anomalies and the best-fit curve. These residuals are not normally distributed, and so $2\sigma[res]$ is not a formal measure of significance, but as the nonlinearity of equation (1) means that the formal measure of significance is complex, then we consider $2\sigma[res]$ to be a suitably simple and universal guide to the goodness of the fit.

[16] The best fitting curve of the simulated 12-month mean maximum global mean surface temperature anomalies with respect to global mean maximum volcanic aerosol optical depth anomaly, using the format of equation (1), is shown in Figure 5 and given by

$$\Delta T = -11.3[1 - \exp(-0.164\tau)]\ K \quad (2)$$

with

$$2\sigma[res] = 0.758\ K \quad (3)$$

It can be seen from the plot and equations (2) and (3) that $2\sigma[res]$ is considerably smaller than $\mathcal{S}$, which gives us confidence that this form of curve is a good fit to the global mean temperature anomalies simulated by HadCM3. As they are, however, entirely based on these HadCM3 simulations they should be applied to real-world eruptions with some caution.

[17] There are considerable differences between equation (2) and the similar relationships between volcanic emissions

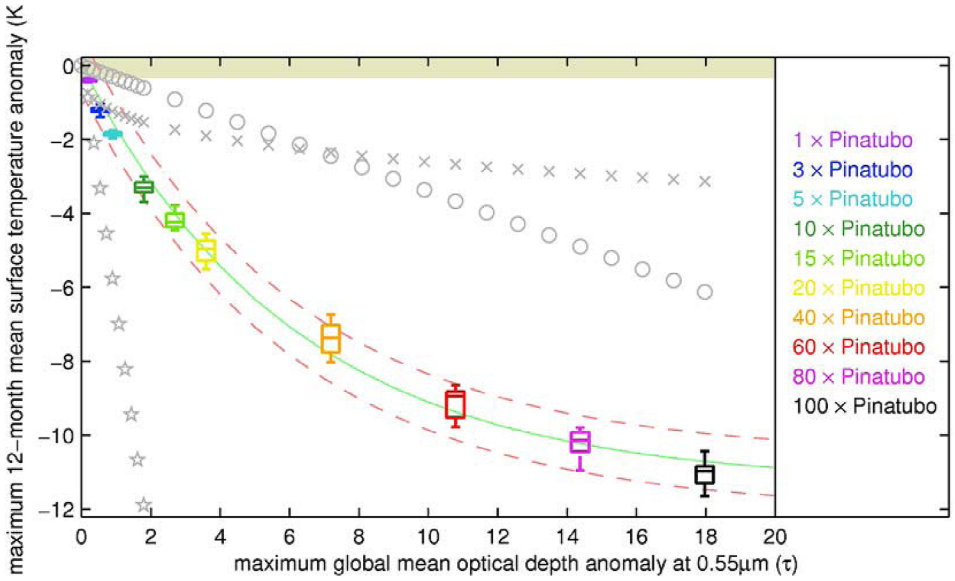

Figure 5. Simple relationship between simulated global mean optical depth anomaly and surface temperature anomalies. The continuous 12-month maximum surface temperature anomalies are plotted here as boxes. The top and bottom of each box shows the interquartile range of temperature anomalies for each month and the central line through the box shows the median value. The whiskers outside the box encompass 95% of the individual temperature anomaly values for the 12-month period. The gray-yellow shading shows 2 standard deviations of control global annual mean temperature anomalies with respect to the climatology of the control. The green line shows the simple scaling relation fitted to the eruption simulation anomalies given in equation (2) and the red dashed lines give two standard deviations of the residuals after fitting given by equation (3). The gray symbols show the simple scaling relations of other authors, *Sigurdsson* [1990] (crosses), *Rampino and Self* [1992] (circles), and *Pollack et al.* [1976] (stars).

and temperature anomalies constructed by other authors [e.g., *Pollack et al.*, 1976; *Rampino and Self*, 1992; *Sigurdsson*, 1990]. The relations constructed by these three authors, shown in gray on Figure 5, are formulated using observed temperature anomalies from a handful of historic eruptions. The relations between eruption size and temperature anomaly constructed by *Pollack et al.* [1976] and *Rampino and Self* [1992] both make the assumption that temperature anomalies scale linearly with eruption size. This linearity is clearly not the case as temperature anomalies following large eruptions are predominantly driven by radiative change and this itself is not a linear function of eruption size nor optical depth. There is some agreement between equation (2) and the simple scaling relation proposed by *Sigurdsson* [1990] for small eruptions and the shape of both curves are similar, however the temperature anomalies predicted by *Sigurdsson* [1990] for eruptions larger than 5 × Pinatubo are much smaller than those simulated. Whether equation (2) is a better way of predicting global mean temperature anomalies following a real-world supervolcanic eruption than the relation of *Sigurdsson* [1990] is not proven, but equation (2) is the closest simple description of GCM-simulated supervolcanic temperature anomalies to date.

3.2. Regional Anomalies

[18] While global mean temperature changes are an important indicator of the impact of volcanic eruptions in comparison to other climate forcing mechanisms, regional changes in temperature can be used to evaluate the impact of large eruptions on local populations as well as in the proximity of paleoclimatic study sites. In order to quantify these regional changes, we repeat the fitting analysis to provide relationships between eruption size and temperature anomaly for each model grid box. In each grid box the continuous 12-month period exhibiting the greatest temperature anomalies is identified within the five years following each eruption and these anomalies are then fitted to equation (1), where τ is the global mean maximum optical depth anomaly as before, to give a value of $\mathcal{S}$ and $\mathcal{V}$ for that particular grid box. The resulting maps of $\mathcal{S}$, $\mathcal{V}$ and the residuals from the fits show the regional-scale variability in these values and are displayed in Figure 6. Note that since the 12 month period exhibiting the greatest temperature anomalies at each point and for each eruption size may be slightly different, Figure 6 does not show the best fit coefficients at a snapshot in time following the eruption. Table 1 summarizes the best-fit values for the large-scale surface regions shown in Figure 7, along with two standard deviations of the control run annual mean temperature anomalies ($2\sigma[ctrl]$), the number of grid boxes averaged to give each value, and the percentage contribution that the values in each region make to the global mean.

[19] A comparison of $2\sigma[res]$ and $2\sigma[ctrl]$ in Figures 6c and 6d and in Table 1 shows that besides a few mainly tropical regions with very little interannual change, the fit to equation (1) for the majority (over 85%) of the surface has residuals with a smaller standard deviation than interannual variability. This suggests that if this relationship is used to

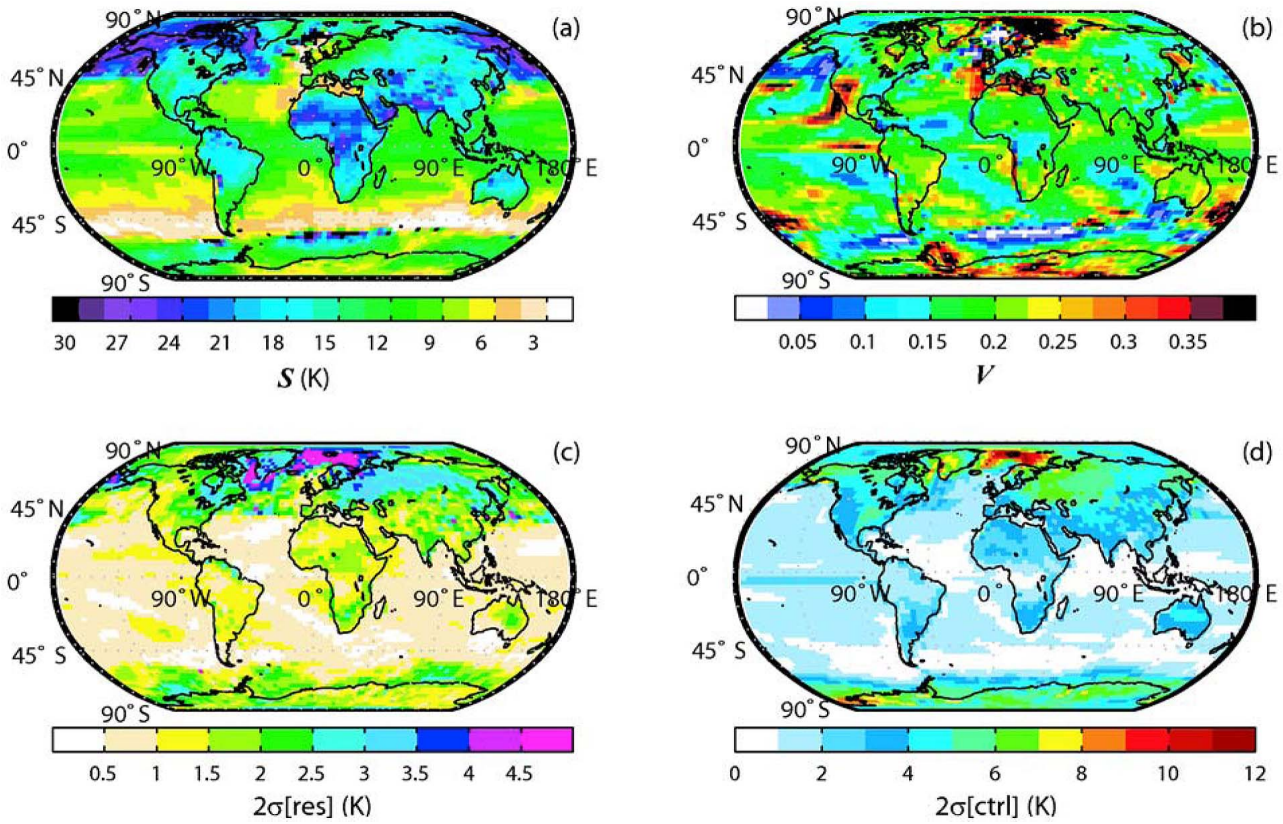

Figure 6. Surface pattern of best-fit coefficients of post-volcanic maximum 12-month mean surface temperature anomalies to equation (1), showing (a) the value of $\mathcal{S}$, (b) the value of $\mathcal{V}$, (c) the goodness of the fit in each region as two standard deviations of the residuals, and (d) interannual variability as two standard deviations of the annual mean surface temperature anomalies in the control run.

Table 1. Mean Values of $\mathcal{S}$, $\mathcal{V}$, $2\sigma[res]$, and $2\sigma[ctrl]$ for the Land Surface Regions Indicated in Figure 7[a]

	Region	$\mathcal{S}$ (K)	$\mathcal{V}$	$2\sigma[res]$ (K)	$2\sigma[ctrl]$ (K)	G	%gm
1	northwestern North America	−21.3	0.15	1.8	4.9	119	1.3
2	northeastern North America	−18.2	0.18	2.4	4.8	116	1.3
3	southwestern North America	−15	0.27	1.5	3.6	45	0.8
4	southeastern North America	−17.5	0.14	2.1	4.6	37	0.7
5	northern Greenland	−15	0.22	2.9	6.1	48	0.2
6	southern Greenland and Iceland	−18.1	0.20	3.4	6.8	21	0.2
7	western and central Europe	−14.3	0.19	2.1	4.4	93	1.5
8	northern Europe and northern Siberia	−14.2	0.24	3.0	5.9	133	1.3
9	northeastern and central Asia	−17.9	0.16	2.4	4.3	183	2.4
10	eastern Siberia	−25.3	0.15	1.9	5.4	47	0.5
11	central and western Asia	−19.2	0.20	1.9	4.8	104	1.7
12	Central America and northern South America	−18.5	0.19	1.5	2.2	46	1.0
13	northern Africa	−21.3	0.18	1.4	2.7	172	3.6
14	Indian Peninsula	−21.9	0.18	1.9	3.6	50	1.0
15	southeastern Asia	−17.8	0.16	1.4	2.0	75	1.6
16	western South America	−18.5	0.19	1.2	1.9	38	0.8
17	eastern South America	−16.4	0.21	1.2	2.2	63	1.4
18	southern South America	−11.9	0.22	1.2	2.9	33	0.6
19	central Africa	−21.2	0.15	1.3	1.5	78	1.8
20	southern Africa	−16.5	0.21	1.6	2.9	55	1.2
21	northwestern Australia	−19.1	0.21	1.4	3.9	28	0.6
22	southwestern Australia	−14.5	0.20	0.9	3.2	20	0.4
23	eastern Australia and New Zealand	−14.4	0.24	1.4	3.4	27	0.5
24	western and central Antarctica	−8.5	0.27	1.6	5.6	572	1.8
25	eastern Antarctica	−11.4	0.19	1.6	6.2	178	0.8

[a]Column G shows the number of model grid boxes averaged to give these values and column %gm shows the percentage contribution of these values in each of the regions to the global mean values.

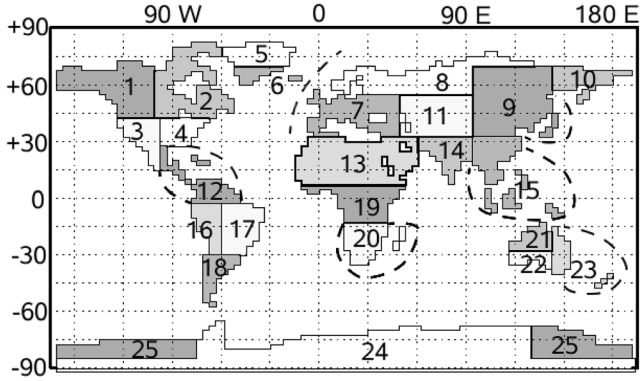

Figure 7. Definition of the regions used in Table 1.

estimate the 12-month mean maximum surface temperature anomaly for an eruption which has not been explicitly simulated in HadCM3, then the greatest source of error in that estimation, for the majority of the globe, would come from natural variability, rather than the error in the fit. This gives us confidence that these regional relations are a means to reconstruct temperature anomalies following generic Pinatubo-like eruptions simulated in HadCM3.

[20] The spatial distribution of $\mathcal{S}$ and $\mathcal{V}$ in Figures 6a and 6b shows the sensitivity of different regions of the globe to volcanically induced temperature changes. The land-sea contrast is evident in $\mathcal{S}$ and this shows, as is to be expected, that even for the very largest aerosol optical depth anomalies, the land surface cools considerably more than the oceans. The highest values of $\mathcal{S}$ are found over the North African and Middle Eastern desert regions, the uniform pattern of $\mathcal{V}$ over these same regions indicates that these are parts of the world which will respond most dramatically to volcanically driven temperature change. This response occurs because the desert regions have a high average insolation and predominantly clear skies, making them very sensitive to decreases in incoming shortwave radiation following a volcanic eruption. The smallest values of $\mathcal{S}$ are found in the oceanic upwelling regions of the Southern Ocean, where relatively warmer surface waters are drawn up from depth and also in the North Atlantic, in both these regions saturation temperature anomalies are no more than −5 K. The North Atlantic response is particularly complex and may be due to the large increases in Meridional Overturning which occur with increasing eruption size in these simulations (see also *Jones et al.* [2005]). The temperature changes predicted for Europe are more moderate than those in the North America and North Asia, which may be due to the relative warmth of the North Atlantic. There is an interesting feature of high V in southwestern North America, which indicates that the region will experience similar temperature anomalies for small as for large eruptions; the reasons for this feature are not clear.

[21] These best fit coefficients $\mathcal{S}$ and $\mathcal{V}$ can be used to populate equation (1) and predict the model temperature response to any magnitude of aerosol optical depth anomaly, including those which have not been explicitly simulated, and this approximation is within a degree or two of the simulations for the 85% of model grid boxes where the residuals are smaller than natural variability. These predictions should, however, be attributed to real historic or prehistoric eruptions with extreme caution. Figure 8 shows the predicted temperature anomalies for a simulation of an eruption with a global mean maximum aerosol optical depth anomaly of $\tau = 1.4$ at 0.55 μm, which may be the maximum optical depth anomaly following the eruption of Mt Tambora in 1815 [*Stothers*, 1984]. Also shown on Figure 8 in dark black/red circles are the peak annual mean temperature anomalies in four different regions between 1816 and 1820, obtained from paleoclimatic records available at the NOAA World Data Center for Paleoclimatology (see Figure 8 caption for references). We have limited our use of these records to those which are complete between 1740 and 1840, as these allow us to calculate two standard deviations of the annual mean temperature anomalies in this 100-year period ($2\sigma[p100]$) for each record. The points surrounded by red circles indicate those records that are greater than $2\sigma[p100]$. The agreement between the paleorecords of annual mean temperature change and the model approximation is good in the studies of the Andes (paleoclimatic data points 3 and 4) where the temperature anomalies are similar to the prediction and greater than $2\sigma[p100]$. The temperature anomalies in the European record are lower than the prediction, however this point lies in a region where natural variability is simulated to be greater than the eruption signal. There is little agreement, however, between the model approximation and the paleo data points in Columbia, US where anomalies are predicted to be the highest in the North American continent and the paleoreconstruction shows moderate cooling which is smaller than $2\sigma[p100]$. In addition to the mean annual values, Figure 8 also shows summer-only temperature anomalies from further paleoclimatic studies in lettered circles outlined in light gray/red. While these values cannot be directly compared to the model output because they are not annual values, they do show lower temperatures than the model on the whole.

[22] There are numerous reasons why the agreement between the prediction and paleoclimatic data shown in Figure 8 should not be excellent. The chief cause of this is probably the incorrect assumption that the distribution and lifetime of stratospheric sulfate aerosol following Tambora is the same as the "Pinatubo-like" model used here. Other model limitations may be the initial conditions chosen or the limited representation of sulfate aerosol chemistry. There may be inaccuracies in the paleoclimatic temperature records which the inclusion of more data would help to address. The effects of the moderately strong 1817 El Nino event [*Ortileb*, 2000] could also be masking part of the cooling signal from Tambora in the paleoclimatic temperature record as found by *D'Arrigo et al.* [2009] for tropical sites, though it is unlikely that this effect is strong in the extratropical regions examined here [*Trenberth and Caron*, 2000]. To investigate these differences further, an obvious second candidate for comparison would be the well-observed anomalies of Pinatubo on which these simulations are based, but as the predicted temperature anomalies for this eruption are indistinct from natural variability a direct comparison would not be robust. Despite their shortcomings, there is still value in these approximations as guides to the possible temperature anomalies across the globe following a volcanic eruption which produces a global mean aerosol optical depth anomaly falling within the range of Pinatubo −100 × Pinatubo.

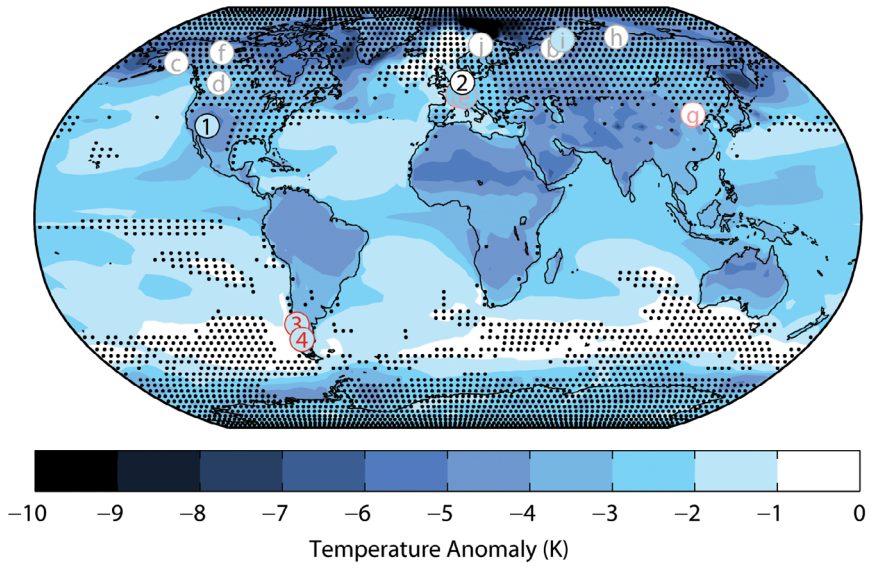

Figure 8. Postvolcanic maximum 12-month mean surface temperature anomalies following a volcanic eruption with a global mean maximum aerosol optical depth anomaly of 1.4 at 0.55 μm - approximately the same as the anomaly following the 1815 Tambora eruption [*Stothers*, 1984], coupled with paleoclimatic studies of the maximum annual mean temperature anomaly between 1816 and 1820. The black dots indicate temperature anomalies which are not predicted to be distinct from natural variability as they are less than two standard deviations of the control annual mean temperature anomalies. The numbered circles are colored with reference to the Figure 8 color bar to show anomalies of paleoclimatic temperature reconstructions between 1816 and 1820 and circles with a red outline indicate that these anomalies are greater than two standard deviations of annual temperature anomalies between 1740 and 1840. The lettered circles with light gray/red outlines show similar data but for summer-only mean values. These different studies are tree ring data from Colorado [*Salzer and Kipfmueller*, 2005] (labeled 1); multiproxy data from Europe, [*Luterbacher et al.*, 2004; *Xoplaki et al.*, 2005] (labeled 2); partially hidden behind 4 (labeled 3); and tree ring data from two locations in the Southern Andes [*Villalba et al.*, 2003] (labeled 4). French grape-harvest dates are labeled a (hidden behind e) *Chuine et al.* [2004]; lake sediments from Baffin Island are labeled b (partially hidden behind i) *Moore et al.* [2001]; tree ring data from the Gulf of Alaska are labeled c *Wiles et al.* [1996]; tree ring data from the Canadian Rockies are labeled d *Luckman and Wilson* [2005]; Swiss grape harvest dates are labeled e (partially hidden behind 2) *Meier et al.* [2007]; tree ring data from northwestern Canada are labeled f *Szeicz and MacDonald* [1995]; stalagmite data from Beijing, China, are labeled g *Tan et al.* [2003]; tree ring data from Taymir, northern Siberia, are labeled h *Jacoby et al.* [2000]; tree ring data from the Yamal Peninsula, Siberia, are labeled i *Hantemirov and Shiyatov* [2002]; tree ring data from Scandinavia are labeled j [*Grudd*, 2008]. All paleoclimate data is archived at the World Data Center for Paleoclimatology, Boulder, Colorado, USA.

[23] An additional feature of the relation shown in equation (1) is that it can be inverted to give an expression for τ if the best-fit values of $\mathcal{S}$ and $\mathcal{V}$ are known. By substituting a measure of the lower temperatures expected from interannual variability (i.e., $-2\sigma[ctrl]$) into this inverted relation in place of ΔT, then we get the following expression for the global mean maximum optical depth increase at which surface temperature anomalies are predicted to exceed two standard deviations of annual mean temperature anomalies.

$$\tau_c = -\frac{-\ln\left[1 - \frac{(-2\sigma[ctrl])}{\mathcal{S}}\right]}{\mathcal{V}} \tag{4}$$

This value has been calculated for each grid box and Figure 9 is a map of τ_c. This map shows that, in HadCM3, temperature anomalies following 1–3 × Pinatubo eruptions are distinct from natural variability in the tropics (excluding the equatorial Pacific) and that only eruptions with a maximum aerosol optical depth anomaly greater than 7–10 × Pinatubo result in distinct temperature anomalies across the midlatitudes. Over large regions of Antarctica only the 20 × Pinatubo eruption or greater has a clear and distinct temperature signal in the model. These results are, of course, based solely on the simulations conducted in HadCM3 and include all the accompanying caveats, but if they can be considered an approximation to real-world behavior then they suggest that paleoclimatic and remote sensing observations of temperature anomalies following large eruptions will be most effective if they are conducted in the tropics.

4. Summary and Discussion

[24] We have derived a set of simple global and regional relationships between Pinatubo-like aerosol optical depth anomalies and resulting surface temperature change simu-

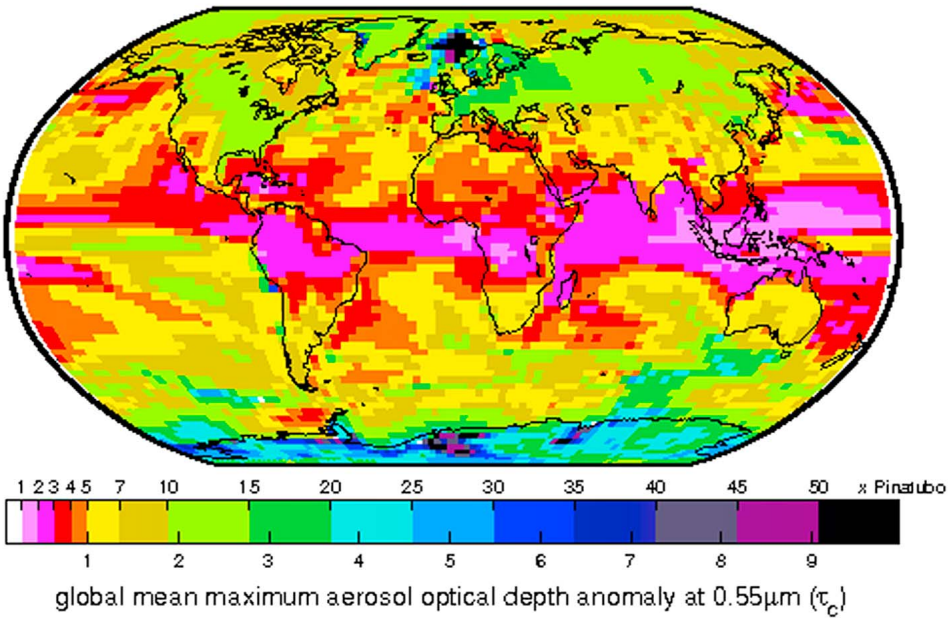

Figure 9. Predicted eruption size at which regional volcanically driven maximum 12-month mean surface temperature anomalies exceed two standard deviations of the climatological annual surface temperatures. This is calculated by inverting the regional simple scaling relations (equation (4)) and finding τ_c for a given ΔT, $\mathcal{S}$ and $\mathcal{V}$. Figure 9 is colored by order of global mean aerosol optical depth anomaly with respect to the Pinatubo eruption and the absolute value of this anomaly is also marked on the lower axis of the color bar for reference.

lated on the GCM HadCM3. We simulated a range of aerosol optical depth anomalies from the size of Pinatubo to 100 × Pinatubo, using the Sato Index as the basis of the spatial and temporal distribution of the anomalies. A simple global mean relationship was found by fitting the maximum 12-month mean global temperature anomalies from these simulations to equation (1). The best fit coefficients were $\mathcal{S} = -11.3$ and $\mathcal{V} = 0.164$ and the residuals from the fit were small. We then used this technique to formulate individual relationships for each model grid box and the resulting spatial pattern of best-fit coefficients are shown in Figure 6. We have shown that these spatial patterns can be used to approximate model temperature anomalies at eruption sizes which have not been explicitly simulated in HadCM3. We have also inverted the simple relationship to estimate the size of volcanic eruption required for a region to experience a temperature anomaly which is distinct from the model's interannual variability. The results of this inversion suggest that paleoclimatic studies in the tropics would be most beneficial when looking for the temperature signals of volcanic eruptions.

[25] As discussed previously, there are a number of caveats that must be considered when applying the data from these idealized simulations to past or potential future eruptions. While the relationship derived here is valid for a wider range of optical depth perturbations than those used to extrapolate from historical eruptions, it is derived using idealized aerosol distributions based on the Pinatubo eruption alone. Thus if the optical depth perturbation from a given volcano is substantially different in microphysical properties (e.g., size, etc.), spatial distribution (resulting from a different location of volcano or different atmospheric circulation patterns), or rates of aerosol formation and sedimentation, then the relationship here may not be appropriate. For example, it was shown in section 2 that the maximum temperature anomalies in the simulations of *Robock et al.* [2009] are greater than the simulations made here and that this difference increases with eruption size. This increase is probably because their model explicitly replicates the conversion of sulphur dioxide to sulfate aerosol in the stratosphere. The timescales associated with this appear to enhance the duration of the aerosol forcing in comparison with the simulations made on HadCM3. Further limitations of the model itself, such as resolution and model top, may also impact these values, though this influence is likely to be small. Despite these caveats relating to the real-world applicability of these simulations, we have demonstrated the use of a widely respected GCM to produce a simple relationship between Pinatubo-like aerosol optical depth anomalies and the maximum 12 month mean surface temperature response and the further applications of such a relationship. As this simulation has only been conducted on the UKMO model HadCM3 to date, then the results presented here are necessarily dependent on that particular model, but the technique of analysis may also be applicable to similar simulations of large radiative forcing scenarios such as geoengineering simulations or global warming experiments.

[26] **Acknowledgments.** We gratefully acknowledge the funding and support of the UK Natural Environment Research Council and the National Center for Atmospheric Science. We would like to thank the British Atmospheric Data Center and the National Center for Atmospheric Research for access to reanalysis data and the National Oceanographic and Atmospheric

Administration for access to paleoclimate temperature proxy data. We would also like to thank three anonymous reviewers for their help in improving this manuscript.

References

Ambrose, S. H. (1998), Late Pleistocene human bottlenecks, volcanic winter, and differentiation of modern humans, *J. Human Evol.*, *34*, 623–651.

Bekki, S. (1995), Oxidation of volcanic SO2: A sink for stratospheric OH and H_2O, *Geophys. Res. Lett.*, *22*(8), 913–916.

Bluth, G., S. Doiron, C. Schnetzler, A. Krueger, and L. Walter (1992), Global tracking of the SO_2 clouds from the June 1991 Mount Pinatubo eruptions, *Geophys. Res. Lett.*, *19*(2), 151–154.

Christiansen, B. (2007), Volcanic eruptions, large-scale modes in the northern hemisphere, and the El Nino southern oscillation, *J. Clim.*, *21*, 910–922.

Chuine, I., P. Yiou, B. Seguin, V. Daux, and E. Le Roy Ladurie (2004), Grape ripening as a past climate indicator, *Nature*, *432*, 289–290.

Collins, M., S. F. B. Tett, and C. Cooper (2001), The internal climate variability of HadCM3, a version of the Hadley Centre coupled model without flux adjustments, *Clim. Dyn.*, *17*(1), 61–81.

Cusack, S., A. Slingo, J. M. Edwards, and M. Wild (1998), The radiative impact of a simple aerosol climatology on the Hadley Centre atmospheric GCM, *Q. J. R. Meteorol. Soc.*, *124*, 2517–2526.

D'Arrigo, R., R. Wilson, and A. Tudhope (2009), The impact of volcanic forcing on tropical temperatures during the past four centuries, *Nat. Geosci.*, *2*, 51–56.

Fischer, E. M., J. Luterbacher, E. Zorita, S. F. B. Tett, C. Casty, and H. Wanner (2007), European climate response to tropical volcanic eruptions over the last half millenium, *Geophys. Res. Lett.*, *34*, L05707, doi:10.1029/2006GL027992.

Gleckler, P. J., K. AchutaRao, J. M. Gregory, B. D. Santer, K. E. Taylor, and T. M. L. Wigley (2006), Krakatoa lives: the effect of volcanic eruptions on ocean heat content and thermal expansion, *Geophys. Res. Lett.*, *33*, L17702, doi:10.1029/2006GL026771.

Gordon, C., C. Cooper, C. A. Senior, H. Banks, J. M. Gregory, T. C. Johns, J. F. B. Mithcell, and R. A. Wood (2000), The simulation of SST, sea ice extents and ocean heat transports in a version of the Hadley Centre coupled model without flux adjustments, *Clim. Dyn.*, *16*, 147–168.

Graf, H. F., I. Kirchner, A. Robock, and I. Schult (1993), Pinatubo eruption winter climate effects: Model versus observations, *Clim. Dyn.*, *9*, 81–93.

Gregory, J. M., W. J. Ingram, M. A. Palmer, G. S. Jones, P. A. Stott, R. B. Thorpe, J. A. Lowe, T. C. Johns, and K. D. Williams (2004), A new method for diagnosing radiative forcing and climate sensitivity, *Geophys. Res. Lett.*, *31*, L03205, doi:10.1029/2003GL018747.

Grudd, H. (2008), Torneträsk tree-ring width and density AD 500–2004: A test of climatic sensitivity and a new 1500-year reconstruction of north Fennoscandian summers, *Clim. Dyn.*, *31*(7), 843–857.

Hansen, J., A. Lacis, R. Ruedy, and M. Sato (1992), Potential climate impact of Mount Pinatubo eruption, *Geophys. Res. Lett.*, *19*, 215–218.

Hantemirov, R., and S. Shiyatov (2002), A continuous multimillennial ring-width chronology in Yamal, northwestern Siberia, *Holocene*, *12*(6), 717–726.

Hegerl, G., F. W. Zwiers, P. Braconnot, N. Gillett, Y. Luo, J. Marengo Orsini, N. Nicholls, J. Penner, and P. Stott (2007), Understanding and attributing climate change, in *Climate Change 2007: The Physical Science Basis. Contribution of Working Group I to the Fourth Assessment Report of the Intergovernmental Panel on Climate Change*, edited by S. Solomon et al., page numbers?, Cambridge Univ. Press, Cambridge, U. K.

Hewitt, C. D., A. J. Broccoli, J. F. B. Mitchell, and R. J. Stouffer (2001), A coupled model study of the last glacial maximum: Was part of the North Atlantic relatively warm?, *Geophys. Res. Lett.*, *27*, 1571–1574.

Houghton, J., Y. Ding, D. Griggs, M. Noguer, P. van der Linden, X. Dai, K. Maskell, and C. Johnson (Eds.) (2001), *Climate Change 2001: The Scientific Basis*, Cambridge Univ. Press, Cambridge, U. K.

Jacoby, G., N. Lovelius, O. Shumilov, O. Raspopov, J. Karbainov, and D. Frank (2000), Long-term temperature trends and tree growth in the Taymir region of northern Siberia, *Quat. Res.*, *53*(3), 312–318.

Johns, T. C., et al. (2003), Anthropogenic climate change for 1860 to 2100 simulated with the HadCM3 model under updated emissions scenarios, *Clim. Dyn.*, *20*, 583–612.

Jones, G., J. Gregory, P. Stott, S. Tett, and R. Thorpe (2005), An AOGCM simulation of the climate response to a volcanic super-eruption, *Clim. Dyn.*, *25*(78), 725–739.

Kirchner, I., G. L. Stenchikov, H. F. Graf, A. Robock, and J. C. Antuna (1999), Climate model simulation of winter warming and summer cooling following the 1991 Mount Pinatubo volcanic eruption, *J. Geophys. Res.*, *104*(D16), 19,053–19,055.

Kodera, K. (1994), Influence of volcanic eruptions on the troposphere through stratospheric dynamical processes in the Northern Hemisphere winter, *J. Geophys. Res.*, *99*(D1), 1273–1282.

Labitzke, K., and H. van Loon (1989), The southern oscillation. Part IX: The influence of volcanic eruptions on the southern oscillation in the stratosphere., *J. Clim.*, *2*, 1223–1226.

Luckman, B., and R. Wilson (2005), Summer temperatures in the Canadian Rockies during the last millennium: A revised record, *Clim. Dyn.*, *24*(2), 131–144.

Luterbacher, J., D. Dietrich, E. Xoplaki, M. Grosjean, and H. Wanner (2004), European seasonal and annual temperature variability, trends, and extremes since 1500, *Science*, *303*(5663), 1499–1503.

McCormick, M. P., L. W. Thomason, and C. R. Trepte (1995), Atmospheric effects of the Mt Pinatubo eruption, *Nature*, *373*, 399–404.

Meier, N., T. Rutishauser, C. Pfister, H. Wanner, and J. Luterbacher (2007), Grape harvest dates as a proxy for Swiss April to August temperature reconstructions back to AD 1480, *Geophys. Res. Lett.*, *34*, L20705, doi:10.1029/2007GL031381.

Minnis, P., E. F. Harrison, L. L. Stowe, G. G. Gibson, F. M. Denn, D. R. Doelling, and W. L. Smith Jr. (1993), Radiative climate forcing by the Mount Pinatubo eruption, *Science*, *259*(5100), 1411–1415.

Moore, J., K. Hughen, G. Miller, and J. Overpeck (2001), Little Ice Age recorded in summer temperature reconstruction from vared sediments of Donard Lake, Baffin Island, Canada, *J. Paleolimnol.*, *25*(4), 503–517.

Niemeier, U., C. Timmreck, H.-F. Graf, S. Kinne, S. Rast, and S. Self (2009), Initial fate of fine ash and sulfur from large volcanic eruptions, *Atmos. Chem. Phys.*, *9*, 9043–9057.

Oppenheimer, C. (2002), Limited global change due to the largest known quaternary eruption, Toba 74 kyr BP, *Quat. Sci. Rev.*, *21*, 1593–1609.

Oppenheimer, C. (2003), Climatic, envronmental and human consequences of the largest known historic eruption: Tambora volcano (Indonesia) 1815, *Progr. Phys. Geogr.*, *27*(2), 230–259.

Ortileb, L. (2000), *El Niño and the Southern Oscillation: Multiscale Variability and Global and Regional Impacts*, pp. 207–295, Cambridge Univ. Press, Cambridge, U. K.

Pinto, J. P., R. P. Turco, and O. B. Toon (1989), Self-limiting physical and chemical effects in volcanic eruption clouds, *J. Geophys. Res.*, *94*(D8), 11,165–11,174.

Pollack, J. B., O. B. Toon, C. Sagan, A. Summers, B. Baldwin, and W. V. Camp (1976), Volcanic explosions and climate change: a theoretical assessment, *J. Geophys. Res.*, *81*, 1071–1083.

Pope, V. D., M. L. Gallani, P. R. Rowntree, and R. A. Stratton (2000), The impact of new physical parametrizations in the Hadley Centre climate model: HadAM3, *Clim. Dyn.*, *16*, 123–146.

Ramachandran, S., V. Ramaswamy, G. L. Stenchikov, and A. Robock (2000), Radiative impact of the Mount Pinatubo volcanic eruption: Lower stratospheric response, *J. Geophys. Res.*, *105*(D19), 24,409–24,429.

Rampino, M., and S. Self (1992), Volcanic winter and accelerated glaciation following the Toba super-eruption, *Nature*, *359*, 50–52.

Rampino, M. R., and S. Self (1993), Climate-Volcanism feedback and the Toba eruption of 74,000 years ago, *Quat. Res.*, *40*, 269–280.

Randall, D. A., et al. (2007), Cilmate models and their evaluation, in *Climate Change 2007: The Physical Science Basis. Contribution of Working Group I to the Fourth Assessment Report of the Intergovernmental Panel on Climate Change*, edited by S. Solomon et al., Cambridge Univ. Press, Cambridge, U. K.

Rind, D., N. K. Balachandran, and R. Suozzo (1992), Climate change and middle atmosphere. Part II: The impact of volcanic aerosols., *J. Clim.*, *5*, 189–208.

Robock, A. (2000), Volcanic eruptions and climate, *Rev. Geophys.*, *38*(2), 191–219.

Robock, A., and J. Mao (1992), Winter warming from large volcanic eruptions, *Geophys. Res. Lett.*, *12*(24), 2405–2408.

Robock, A., C. Ammann, L. Oman, D. Shindell, S. Levis, and G. Stenchikov (2009), Did the Toba volcanic eruption of 74 ka B.P. produce widespread glaciation?, *J. Geophys. Res.*, *114*, D10107, doi:10.1029/2008JD011652.

Salzer, M., and K. Kipfmueller (2005), Reconstructed temperature and precipitation on a millennial timescale from tree-rings in the southern Colorado plateau, U.S.A., *Clim. Change*, *70*(23), 465–487, doi:10.1007/s10584-005-5922-3.

Santer, B., T. Wigley, C. Doutriaux, J. Boyle, J. Hansen, P. Jones, G. Meehl, E. Roeckner, S. Sengupta, and K. Taylor (2001), Accounting for the effects of volcanoes and ENSO in comparisons of modeled and observed temperature trends, *J. Geophys. Res.*, *106*, 28,033–28,060, doi:10.1029/2000JD000189.

Sato, M., J. E. Hansen, M. P. McCormick, and J. B. Pollack (1993), Stratospheric aerosol optical depths, 1850-1990, *J. Geophys. Res.*, *98*(D12), 22,987–22,994.

Schneider, D. P., C. M. Ammann, B. L. Otto-Bliesner, and D. S. Kaufman (2009), Climate response to large, high-latitude and low-latitude volcanic eruptions in the Community Climate System Model, *J. Geophys. Res.*, *114*, D15101, doi:10.1029/2008JD011222.

Seber, G., and C. Wild (2003), *Nonlinear Regression*, John Wiley, Hoboken, N. J.

Shindell, D. T., G. A. Schmidt, M. E. Mann, and G. Faluvegi (2004), Dynamic winter climate response to large tropical volcanic eruptions since 1600, *J. Geophys. Res.*, *109*, D05104, doi:10.1029/2003JD004151.

Sigurdsson, H. (1990), Evidence of volcanic loading of the atmosphere and climate response, *Global Planet. Change*, *3*, 277–289.

Slingo, A. (1989), A GCM parameterization for the shortwave radiative properties of water clouds, *J. Atmos. Sci.*, *46*(10), 1419–1427.

Solomon, S., D. Qin, M. Manning, Z. Chen, M. Marquis, K. Averyt, M. Tignor, and H. Miller (Eds.) (2008), *Climate Change 2007: The Physical Science Basis*, Cambridge Univ. Press, Cambridge, U. K.

Stainforth, D. A., et al. (2005), Uncertainty in prediction of the climate response to rising levels of greenhouse gases, *Nature*, *433*, 403–406.

Stenchikov, G., I. Kirchner, A. Robock, H. F. Graf, J. C. Antuna, R. G. Grainger, A. Lambert, and L. Thomason (1998), Radiative forcing from the 1991 Mount Pinatubo volcanic eruption, *J. Geophys. Res.*, *103*(D12), 13,837–13,857.

Stenchikov, G., A. Robock, V. Ramaswamy, M. Schwarzkopf, K. Hamilton, and S. Ramachandran (2002), Arctic Oscillation response to the 1991 Mount Pinatubo eruption: Effects of volcanic aerosols and ozone depletion, *J. Geophys. Res.*, *107*(D24), 4803, doi:10.1029/2002JD002090.

Stenchikov, G., K. Hamilton, R. J. Stouffer, A. Robock, V. Ramaswamy, B. Santer, and H.-F. Graf (2006), Arctic Oscillation response to volcanic eruptions in the IPCC AR4 climate models, *J. Geophys. Res.*, *111*, D07107, doi:10.1029/2005JD006286.

Stothers, R. B. (1984), The great Tambora eruption in 1815 and its aftermath, *Science*, *224*, 1191–1198.

Stott, P., S. F. B. Tett, G. S. Jones, M. R. Allen, J. F. B. Mitchell, and G. J. Jenkins (2000), External control of 20th century temperature by natural and anthropogenic forcing, *Science*, *290*, 2133–2137.

Szeicz, J., and G. MacDonald (1995), Dendroclimatic reconstruction of summer temperatures in northwestern Canada since AD 1638 based on age-dependent modeling, *Quat. Res.*, *44*(2), 257–266.

Tan, M., T. Liu, J. Hou, X. Qin, H. Zhang, and T. Li (2003), Cyclic rapid warming on centennial-scale revealed by a 2650-year stalagmite record of warm season temperature, *Geophys. Res. Lett.*, *30*(12), 1617, doi:10.1029/2003GL017352.

Tett, S. F. B., et al. (2002), Estimation of natural and anthropogenic contributions to 20th century temperature change, *J. Geophys. Res.*, *107*(D16), 4306, doi:10.1029/2000JD000028.

Thordarson, T., and S. Self (2003), Atmospheric and environmental effects of the 1783–1784 Laki eruption: A review and reassessment, *J. Geophys. Res.*, *108*(D1), 4011, doi:10.1029/2001JD002042.

Timmreck, C., and H. F. Graf (2000), A microphysical model for simulation of stratospheric aerosol in a climate model, *Meteorol. Z.*, *9*(5), 263–282.

Timmreck, C., H. F. Graf, and J. Feichter (1999), Simulation of Mt Pinatubo volcanic aerosol with the Hamburg climate model ECHAM4, *Theor. Appl. Climatol.*, *62*, 85–108.

Timmreck, C., S. Lorenz, T. Crowley, S. Kinne, T. Raddatz, M. Thomas, and J. Jungclaus (2009), Limited temperature response to the very large AD 1258 volcanic eruption, *Geophys. Res. Lett.*, *36*, L21708, doi:10.1029/2009GL040083.

Trenberth, K., and J. Caron (2000), The Southern Oscillation revisited: Sea level pressures, surface temperatures, and precipitation, *J. Clim.*, *13*, 4358–4365.

Turner, A. G., P. M. Inness, and J. M. Slingo (2005), The role of the basic state in the ENSO-monsoon relationship and implications for predictability, *Q. J. R. Meteorol. Soc.*, *131*(607), 781–804.

Villalba, R., A. Lara, J. Boninsegna, M. Masiokas, S. Delgado, J. Aravena, F. Roig, A. Schmelter, A. Wolodarsky, and A. Ripalta (2003), Large-scale temperature changes across the southern Andes: 20th-century variations in the context of the past 400 years, *Clim. Change*, *59*(1), 177–232.

Wiles, G., R. D'Arrigo, and G. Jacoby (1996), Temperature changes along the Gulf of Alaska and the Pacific Northwest coast modeled from coastal tree rings, *Can. J. Forest Res.*, *26*(3), 474–481.

Wolter, K., and M. S. Timlin (1998), Measuring the strength of ENSO events - how does 1997/98 rank?, *Weather*, *53*, 315–324.

World Meteorological Organization (1983), Report of the experts meeting on aerosols and their climatic effects, *Rep. WCP-55*, Geneva, Switzerland.

Xoplaki, E., J. Luterbacher, H. Paeth, D. Dietrich, N. Steiner, M. Grosjean, and H. Wanner (2005), European spring and autumn temperature variability and change of extremes over the last half millennium, *Geophys. Res. Lett.*, *32*, L15713, doi:10.1029/2005GL023424.

Zielinski, G. A., L. D. Mayewski, S. Whitlow, M. Twickler, and K. Taylor (1996), Potential atmospheric impact of the Toba mega-eruption 71,000 years ago, *Geophys. Res. Lett.*, *23*(8), 837–840.

B. M. Harris and E. J. Highwood, Department of Meteorology, University of Reading, Earley Gate, PO Box 243, Reading RG6 6BB, UK. (bethanmary@gmail.com; e.j.highwood@reading.ac.uk)